

# Dwarf galaxies in voids: Suppressing star formation with photo-heating

Matthias Hoeft<sup>1</sup>, Gustavo Yepes<sup>2</sup>, Stefan Gottlöber<sup>3</sup>, and Volker Springel<sup>4</sup>

<sup>1</sup>*International University Bremen, Campus Ring 1, 28759 Bremen, Germany*

<sup>2</sup>*Grupo de Astrofísica, Universidad Autónoma de Madrid, Cantoblanco, 28039 Madrid, Spain*

<sup>3</sup>*Astrophysikalisches Institut Potsdam, An der Sternwarte 16, 14482 Potsdam, Germany*

<sup>4</sup>*Max-Planck-Institut für Astrophysik, Karl-Schwarzschild-Str. 1, Garching bei München, Germany*

## ABSTRACT

We study structure formation in cosmological void regions using high-resolution hydrodynamical simulations. Despite being significantly underdense, voids are populated abundantly with small dark matter halos which should appear as dwarf galaxies if their star formation is not suppressed significantly. We here investigate to which extent the cosmological UV-background photo-evaporates baryons out of halos of dwarf galaxies, and thereby limits their cooling and star formation rates. Assuming a Haardt & Madau UV-background with reionisation at redshift  $z = 6$ , our samples of simulated galaxies show that halos with masses below a characteristic mass of  $M_c(z = 0) = 6.5 \times 10^9 h^{-1} M_\odot$  are baryon-poor, but in general not completely empty, because baryons that are in the condensed cold phase or are already locked up in stars resist evaporation. In halos with mass  $M \lesssim M_c$ , we find that photo-heating suppresses further cooling of gas. The redshift and UV-background dependent characteristic mass  $M_c(z)$  can be understood from the equilibrium temperature between heating and cooling at a characteristic overdensity of  $\delta \simeq 1000$ . If a halo is massive enough to compress gas to this density despite the presence of the UV background, gas is free to ‘enter’ the condensed phase and cooling continues in the halo, otherwise it stalls. By analysing the mass accretion histories of dwarf galaxies in voids, we show that they can build up a significant amount of condensed mass at early times before the epoch of reionisation. Later on, the amount of mass in this phase remains roughly constant, but the masses of the dark matter halos continue to increase. Consequently, photo-heating leads to a reduced baryon fraction in void dwarf galaxies, endows them with a rather old stellar population, but still allows late star formation to some extent. We estimate the resulting stellar mass function for void galaxies. While the number of galaxies at the faint end is significantly reduced due to photo-heating, additional physical feedback processes may be required to explain the apparent paucity of dwarfs in observations of voids.

**Key words:** cosmology: theory – methods: numerical – galaxies: evolution – galaxies: formation

## 1 INTRODUCTION

Large regions of space that contain few or no galaxies can be clearly identified in modern spectroscopic redshift surveys. About 25 years ago, such ‘voids’ have been first discovered (Gregory & Thompson 1978; Joeveer et al. 1978; Kirshner et al. 1981), but it remains a challenge to explain why they are apparently so empty.

It is well known that hierarchical models of structure formation in standard cold dark matter (CDM) cosmologies produce large underdense regions in the distribution of matter (Peebles 1982; Hoffman & Shaham 1982;

van de Weygaert & van Kampen 1993), but these underdense regions still contain structural elements and bound halos, even though the characteristic masses of these objects are several orders of magnitude smaller than corresponding ones found in average regions of the universe. Gottlöber et al. (2003) predicted that a typical  $20 h^{-1}$  Mpc diameter void should contain up to 1000 halos with mass  $\sim 10^9 h^{-1} M_\odot$  and still about 50 halos with mass  $\sim 10^{10} h^{-1} M_\odot$ . Assuming a magnitude of  $M_B = -16.5$  for the galaxy hosted by a halo of mass  $3.6 \times 10^{10} h^{-1} M_\odot$  (Mathis & White 2002), they predict that about five such

galaxies should be found in the inner regions of a typical void of diameter  $20 h^{-1}$  Mpc.

Over the last decade, there were many attempts to find dwarf galaxies in voids (Lindner et al. 1996; Popescu et al. 1997; Kuhn et al. 1997; Grogin & Geller 1999). An overall conclusion from these studies has been that faint galaxies do not tend to fill up the voids outlined by the bright galaxies. Peebles (2001) pointed out that the dwarf galaxies in the Optical Redshift Survey (ORS) follow the distribution of bright galaxies remarkably closely. Using the SDSS data release 2, Goldberg et al. (2004) measured the mass function of galaxies that reside in underdense regions. They selected galaxies as void members if they had less than three neighbours in a sphere with radius  $7 h^{-1}$  Mpc. More than one thousand galaxies passed their selection criterion (which differs slightly from the criterion used in the numerical simulations of Gottlöber et al. (2003) and in this paper). Their measurements are consistent with the predictions from the numerical simulations once the tendency of more massive halos to concentrate at the outer parts of voids (where they still may pass the nearest neighbour selection criterion) is taken into account. However, the observational situation is unclear for halo masses smaller than  $\sim 10^{10} h^{-1} M_{\odot}$ . At present, there are no observational hints that a huge number of dwarf galaxies in voids may exist, despite the large number of small halos predicted by CDM models.

This finding resembles the ‘substructure problem’ in galactic halos (Klypin et al. 1999; Moore et al. 1999). A solution for both problems could arise from physical processes capable of suppressing star formation in dwarf galaxies. The two major effects proposed in this context are supernova feedback and heating of the gas in halos by the UV-background radiation. The latter increases the thermal pressure, and as a result, the gas in systems with  $T_{\text{vir}} \lesssim 10^4 - 10^5$  K can be evaporated out of halos (Umemura & Ikeuchi 1984; Dekel & Rees 1987; Efstathiou 1992; Babul & Rees 1992). Similarly, supernova feedback could drive a galactic outflow that removes a significant fraction of the gas in a dwarf galaxy (Dekel & Silk 1986; Couchman & Rees 1986). However, the efficiency of supernova driven winds depends strongly on the details of model assumptions (Navarro & Steinmetz 1997, 2000; Springel & Hernquist 2003). A general result is that low-mass systems are much more easily affected by supernova driven winds than larger ones (Mac Low & Ferrara 1999; Navarro & Steinmetz 2000).

During the epoch of reionisation, the gas temperature is raised to a few times  $10^4$  K. Rees (1986) argued that in dark matter halos with virial velocities around  $\sim 30 \text{ km s}^{-1}$  gas can then be confined in a stable fashion, neither able to escape nor able to settle to the centre by cooling. The gas in significantly smaller systems is thought to be virtually evaporated (Thoul & Weinberg 1996; Barkana & Loeb 1999). However, due to central self-shielding the evaporation of gas that has already cooled can be significantly delayed (Susa & Umemura 2004b,a). Using radiative transfer simulations, Susa & Umemura (2004a) pointed out that halos may contain a significant amount of stellar mass produced before reionisation occurred, even if their remaining gas mass is evaporated during reionisation.

In a 3D Eulerian adaptive mesh refinement simulation, Tassis et al. (2003) found that the global star formation

rate was significantly reduced during the reionisation epoch. Their result also indicated that stellar feedback enhances this effect dramatically. Thus, an imprint of the epoch of reionisation may be expected for the stellar population in dwarf galaxies. Indeed, almost all dwarf galaxies appear to have an early epoch of star formation (Mateo 1998), but there is no distinct time at which star formation becomes generally suppressed (Grebel & Gallagher 2004). We also note that dark matter halos of dwarf galaxy size are thought to be the formation sites of the first stars (Couchman & Rees 1986; Abel et al. 2000). However, these halos are unlikely to be located in regions that develop into voids, rather they should be found in slightly overdense regions where structure develops faster than in a mean region of the universe.

In this paper, we use high-resolution hydrodynamical simulations of cosmological void regions to analyse the star formation and cooling processes of void galaxies. In particular, the simulations are well suited for studying the evolution of isolated dwarf galaxies from the epoch before reionisation to the present. This allows us to examine whether the UV background has a sufficiently strong effect on dwarf galaxies, keeping them faint enough such that their abundance can be reconciled with observations. We also determine the characteristic mass scale below which cooling is suppressed by the UV background. An analysis of the spatial distribution of dwarfs, the impact of supernova feedback, and the spectral properties of the stellar content of the formed dwarf galaxies will be discussed separately.

Our study is organised as follows. Details of our simulations are described in Section 2. In Section 3, we analyse first the baryon fraction as a function of both halo mass and redshift. Then we investigate the mass growth of the condensed phase. We identify the characteristic mass below which halos are subject to evaporation. Finally, we estimate the galaxy mass function in void regions. We discuss and summarise our results in Section 4.

## 2 SIMULATIONS

### 2.1 Numerical method

Our simulations have been run with an updated version of the parallel Tree-SPH code GADGET (Springel et al. 2001). The code uses an entropy-conserving formulation of SPH (Springel & Hernquist 2002) which alleviates problems due to numerical over-cooling. The code also employs a new algorithm based on the Tree-PM method for the  $N$ -body calculations which speeds up the gravitational force computation significantly compared with a pure tree algorithm. Radiative cooling processes for an optically thin primordial mix of helium and hydrogen are included, as well as photo-ionisation by an external spatially uniform UV-background.

The physics of star formation is treated in the code by means of a sub-resolution model in which the gas of the interstellar medium (ISM) is described as a multiphase medium of hot and cold gas (Yepes et al. 1997; Springel & Hernquist 2003). Cold gas clouds are generated due to cooling and are the material out of which stars can be formed in regions that are sufficiently dense. Supernova feedback heats the hot phase of the ISM and evaporates cold clouds, thereby establishing a self-regulation cycle for star formation. The

heat input due the supernovae also leads to a net pressurisation of the ISM, such that its effective equation of state becomes stiffer than isothermal. This stabilises the dense star forming gas in galaxies against further gravitational collapse, and allows converged numerical results for star formation even at moderate resolution. We also follow chemical enrichment associated with star formation, but we have neglected metal-line cooling in computing the cooling function. See Springel & Hernquist (2003) for a more detailed description of the star formation model implemented in the GADGET code.

## 2.2 Initial conditions

Using the mass refinement technique described by Klypin et al. (2001), we simulate void regions with high mass resolution, embedded in a proper cosmological environment. Our voids have been selected for resimulation from two periodic computational boxes of side-lengths  $L = 80 h^{-1}$  Mpc and  $50 h^{-1}$  Mpc, respectively. To construct suitable initial conditions, we first created an unconstrained random realization at very high resolution, using the  $\Lambda$ CDM power spectrum of perturbations. For the large box,  $N = 1024^3$  particles were used, while for the smaller box, we employed  $2048^3$  ( $\sim 8.6$  billion) particles. The initial displacements and velocities of the particles were calculated using all waves ranging from the fundamental mode  $k = 2\pi/L$  to the Nyquist frequency  $k_{Ny} = 2\pi/L \times N^{1/3}/2$ . To produce initial conditions at lower resolution than this basic high-resolution particle set-up, we then merged particles, assigning to merged particles a velocity and a displacement equal to the average values of the original small-mass particles.

In this way, we first run  $128^3$  low-resolution simulations until the present epoch and selected the void regions from them. The algorithm for identifying the voids is described in detail in Gottlöber et al. (2003). It allows us to select void regions with arbitrary shape. To this end, the method starts from a spherical representation of the void which is then extended by spheres of smaller radius, which are added from the surface of the void into all possible directions. However, in the present application we have restricted the resimulation to a spherical void region to avoid ambiguities in the definition of allowed deviations from spherical shape.

In the second simulation step we use the original sample of small-mass particles in the regions of interest when we construct initial conditions. Thus we reach a mass resolution within the void regions that corresponds to the  $1024^3$  or  $2048^3$  set-up, respectively. We use a series of shells around the voids where we progressively merge more and more of the particles until the effective resolution of  $128^3$  particles is reached again far away from the voids. This procedure ensures that the voids evolve in the proper cosmological environment and with the right gravitational tidal fields. Mixing of particles of different mass occurs only in the shells surrounding the high resolution voids. Finally, we split the particles in the regions of high mass resolution into dark matter and gas particles. For all simulations, we adopted a concordance cosmological model with  $\Omega_m = 0.3$ ,  $\Omega_\Lambda = 0.7$ ,  $\Omega_b = 0.04$ ,  $h = H_0/(100 \text{ km s}^{-1} \text{ Mpc}^{-1}) = 0.7$  and  $\sigma_8 = 0.9$ .

## 2.3 Simulation runs

Using the multi-mass technique described above, we have re-simulated a void region in the  $80 h^{-1}$  Mpc box with three levels of refinement. The mass of a dark matter particle in the void is  $3.4 \times 10^7 h^{-1} M_\odot$ . The corresponding SPH gas particles have an initial mass of  $5.5 \times 10^6 h^{-1} M_\odot$ . Note that some gas particles may reduce their mass during the run (or vanish entirely) if they undergo star formation and create new collisionless star particles. In our analysis of the simulation results, we in general only consider halos composed of a minimum of 150 dark matter particles. For the  $80 h^{-1}$  Mpc simulations this corresponds to a minimum halo mass of  $5.1 \times 10^9 h^{-1} M_\odot$  and a circular velocity  $\sim 23$  km/s.

We have also carried out re-simulations of a void region in the  $50 h^{-1}$  Mpc box. This leads to a substantially improved mass resolution with the same level of refinement. Here we achieve a mass resolution of  $8.2 \times 10^6 h^{-1} M_\odot$  for the dark matter particles, corresponding to a minimum halo mass of  $1.2 \times 10^9 h^{-1} M_\odot$ . In addition, we have evolved this region also with the full resolution available based on the initial high-resolution particle set-up (the  $2048^3$  particle grid, corresponding to four levels of refinement). In this case, the mass resolution is improved to  $1.0 \times 10^6 h^{-1} M_\odot$  for the dark matter particles, and the minimum halo mass reaches down to  $1.6 \times 10^8 h^{-1} M_\odot$ . We give an overview of our simulations in Table 1, where we also list the main simulation parameters.

We follow Power et al. (2003) and set the gravitational softening length for all simulations to the maximum between  $2 h^{-1}$  kpc comoving and  $0.8 h^{-1}$  kpc physical. For the very high-resolution run, the parameters  $1 h^{-1}$  kpc and  $0.5 h^{-1}$  kpc, respectively, are used. We have imposed a minimum SPH smoothing length equal to the gravitational softening length.

In order to analyse in more detail the effects of the UV-background on the baryonic content of halos, we have also carried out several additional runs of our basic simulation of the void identified in the  $50 h^{-1}$  Mpc box. Here we used different choices for the star formation and feedback parameters, and three different values of the UV-flux normalisation, spanning two orders of magnitude in dynamic range. We also ran the same simulation without thermal stellar feedback. Using this run we can demonstrate that thermal feedback itself has only a minor impact on the halo baryon fraction. For all simulations with star formation and feedback, we selected similar parameters for the multiphase model of the ISM as used by Springel & Hernquist (2003). However, we here have not included kinetic feedback (wind model) from supernova, since then it would be very difficult to disentangle the effects caused by the UV background from those caused by supernova driven winds.

The simulations were performed on parallel supercomputers, an IBM Regatta p690 (Jülich Supercomputer Center, Germany), a SGI Altix 3700 (CIEMAT, Spain) and on several different Beowulf PC clusters at the AIP and IU Bremen. The typical CPU time for a simulation with up to 5 million particles was  $\sim 9$  CPU days on an SGI ALTIX with 32 processors. The highest resolution simulation with 44 million particles was run on an AMD Opteron beowulf cluster and took a little less than 2 months of CPU time using 64 processors.

SIMULATION NAME	Refinement levels	$M_{\text{gas}}$	$M_{\text{dark}}$	Particle number	Star fraction	Feedback parameters			
		$(10^6 h^{-1} M_{\odot})$	$(10^6 h^{-1} M_{\odot})$			$\beta$	A	$T_{SN}$	$J_0^{\text{UV}}$
void2	3	5.51	34.2	5,068,359	0.060	0.1	1000	$10^8$	0.95
basic	3	1.50	8.24	7,376,094	0.048	"	"	"	"
high-res	4	0.18	1.03	43,544,537	0.053	"	"	"	"
high-UV	3	1.50	8.24	7,420,759	0.028	"	"	"	9.5
low-UV	3	"	"	7,549,325	0.049	"	"	"	0.095
no-feedback	3	"	"	7,384,373	0.045	0	0	0	0.95

**Table 1.** Main characteristics of the void simulations.  $M_{\text{gas}}$  and  $M_{\text{dark}}$  denote the mass of a gas and of a dark matter particle in the simulation, respectively. Feedback parameters are according to model described in Springel & Hernquist (2003). The UV-flux,  $J_0^{\text{UV}}$ , at  $z = 0$  is given in units of  $10^{-23} \text{ ergs s}^{-1} \text{ cm}^{-2} \text{ sr}^{-1} \text{ Hz}^{-1}$ .

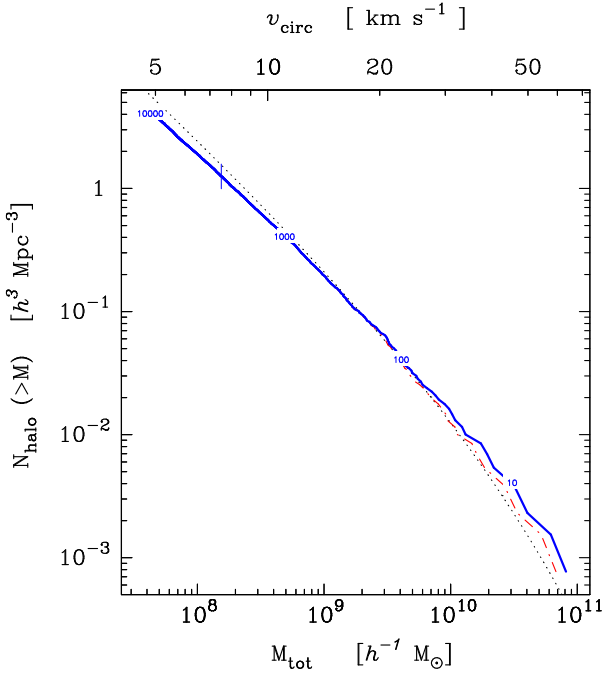


**Figure 1.** Mass function  $n(> M)$  for our basic run halo sample at  $z = 0$ . The mass function is derived by taking into account the total mass within the virial radius. The small vertical line indicates a mass of 150 dark matter particles, which we consider as a lower limit for an acceptable resolution. The numbers along the line indicate the actual number of halos. The dashed line is obtained by considering the dark matter mass instead of the total mass. For comparison the modified Sheth-Tormen mass function derived by Gottl ber et al. (2003) is shown (dotted line). For our halo sample, the circular velocity  $v_{\text{circ}} = GM_{\text{tot}}/r_{\text{vir}}$  can be well approximated by  $v_{\text{circ}} = 31 \text{ km s}^{-1} \times (M_{\text{tot}}/10^{10} h^{-1} M_{\odot})^{0.34}$ .

### 3 SIMULATED DWARF GALAXIES IN VOIDS

#### 3.1 Halo mass function

We identify virialized halos using the Bound Density Maxima (BDM) algorithm (Klypin et al. 1999). In this method, galaxy halos are found from local density maxima with an iterative procedure to identify the centre of mass in a small sphere around the centre. Then, radial density profiles are computed. Particles that are not gravitationally bound to the system are excluded in the computation of the total mass. The radius of the system is selected as the minimum between the virial radius and the point at which the density profile stops declining (e.g. because a nearby halo is encoun-

tered, or the halo lies within another halo). We define the virial radius as the radius where the enclosed mean density equals the value expected for a top-hat collapse model,

$$\frac{M_{\text{vir}}}{4/3 \pi r_{\text{vir}}^3} = \Delta_c(z) \langle \rho \rangle, \quad (1)$$

where  $\langle \rho \rangle$  is the mean cosmic matter density. For the case of a flat cosmology with  $\Omega_m + \Omega_{\Lambda} = 1$ , a useful approximation for the redshift dependent characteristic virial overdensity is given by Bryan & Norman (1998):

$$\Delta_c(z) = \frac{178 + 82x(z) - 39x^2(z)}{1 + x(z)}, \quad (2)$$

$$x(z) = -\frac{1 - \Omega_m}{\Omega_m(1+z)^3 + (1 - \Omega_m)}. \quad (3)$$

The mean density  $\langle \rho \rangle$  evolves with redshift as

$$\langle \rho \rangle(z) = (1+z)^3 \Omega_m \rho_{\text{crit},0} = (1+z)^3 \Omega_m \frac{3H_0^2}{8\pi G}. \quad (4)$$

In low density regions, the number of interacting halos or halos with substructure is very small. Thus, the radii of virtually all our objects correspond to their spherical-overdensity virial radii. For the same reason, the fraction of unbound particles in the halos is small. Hence, we can simply consider all particles within the virial radius to compute further halo properties.

In Figure 1, we show the cumulative mass function for our sample of void halos, based on the measured total virial masses. For comparison, we also include a line for the dark matter halo mass function alone, which however shows appreciable differences only for the most massive halos. Gottl ber et al. (2003) derived a modified Sheth-Tormen mass function for halo populations in underdense regions. They showed that the mass function can be derived from the mean density,  $\Omega_{m,\text{void}}$ , in the volume considered. For our halo sample analysed here (based on the high-res run), the relevant mean density amounts to  $\Omega_{m,\text{void}} \simeq 0.03$ . The predicted mass function for this value is in good agreement with the one measured for the simulated halo sample. Our simulations thus are in good agreement with conclusion obtained in previous works: Voids are filled with a significant number of halos with masses  $M \lesssim 10^{10} h^{-1} M_{\odot}$ . If each of these halos contains the mean cosmic baryon fraction, and cooling and star formation within them is not suppressed significantly, a high density of luminous dwarf galaxies should be expected in voids.

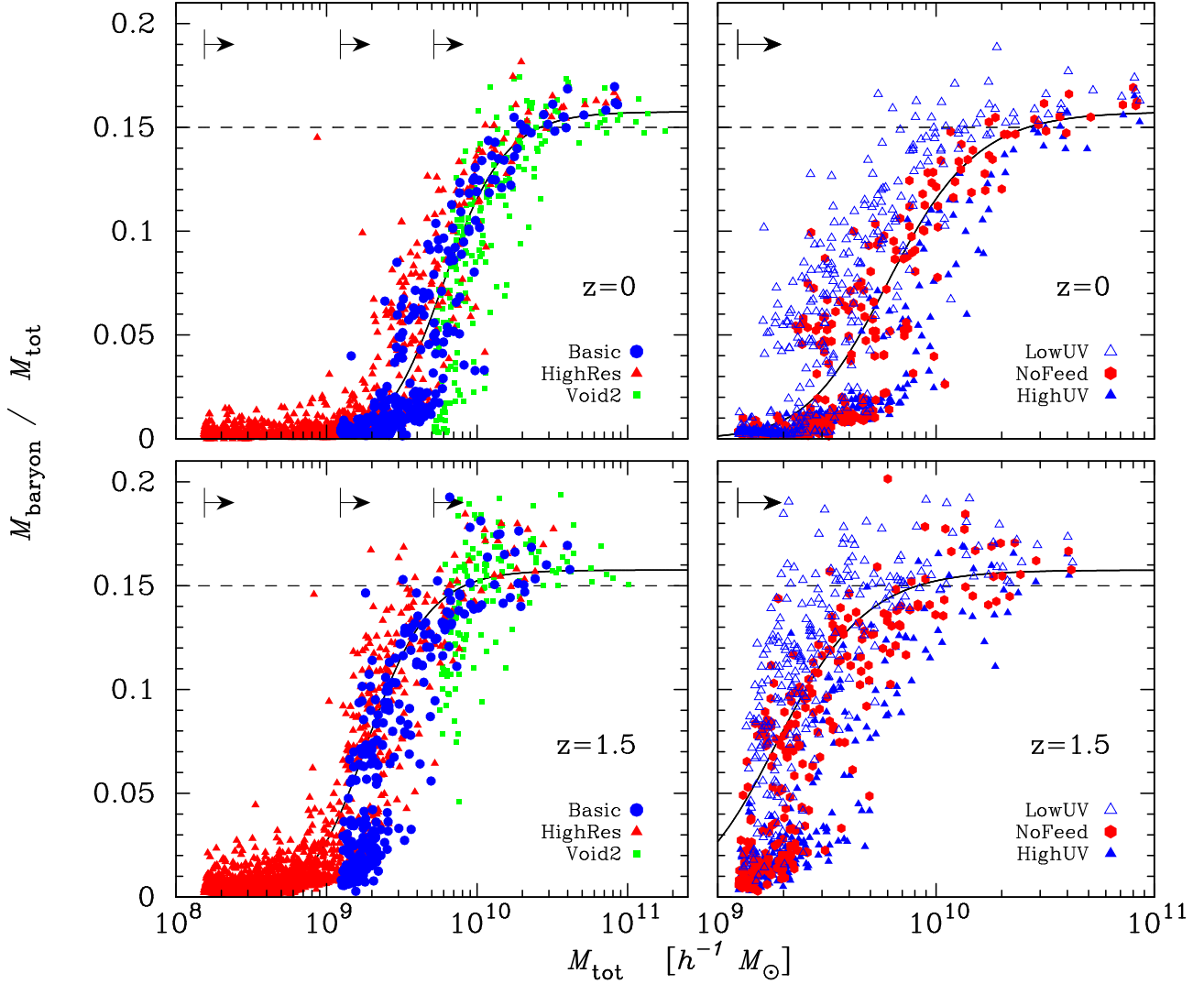


**Figure 2.** The baryon fraction in individual halos. The left panels show the baryon fraction at  $z = 0$  and at  $z = 1.5$  for simulations with different resolution. We consider for each resolution only halos with more than 150 dark matter particles. The corresponding masses are indicated by the arrows at the top. For the high-res run we approximate the baryon fraction for both redshifts by Eq. (5) (solid lines). Right panels show the baryon fractions from simulations with  $10\times$  reduced UV-flux (open triangles), no stellar feedback (filled squares), and  $10\times$  increased flux (filled triangles), respectively. For comparison, we also show the result from a fit to the high-res run (solid line). The dashed line indicates the mean cosmic baryon fraction.

### 3.2 Baryon content of dwarf galaxies

In Figure 2, we show the baryonic mass fraction,  $f_b = M_{\text{baryon}}(< r_{\text{vir}})/M_{\text{tot}}(< r_{\text{vir}})$ , for each halo identified in our simulated voids. The more massive halos in our sample,  $M_{\text{tot}} \gtrsim 2 \times 10^{10} h^{-1} M_{\odot}$ , have approximately the cosmic mean baryon fraction,  $f_{b,\text{cosm}} = \Omega_b/\Omega_m$ , at  $z = 0$ . However, for smaller halos, the baryon fraction decreases rapidly with decreasing halo mass. In fact, most of the smallest halos are nearly free of baryons.

We have checked that insufficient numerical resolution is not the origin of the baryon deficiency measured here for low mass halos. It is particularly important to examine potential numerical effects carefully in this context, because a too small number of resolution elements per halo may introduce a spurious reduction of baryons due to numerical oversmoothing. However, the resolution study presented in

the left panels of Fig. 2 shows that this is not the case: The baryon fractions of the three simulations with different resolutions overlap nicely at redshift  $z = 0$ , as well as at  $z = 1.5$ . We limit ourselves here and in our further analysis to halos with at least 150 dark matter particles in order to protect against effects of numerical resolution in our measurements of the baryon content of halos.

We find that the baryon fraction is insensitive to the details of the definition of the virial radius of halos, because the cumulative baryon fraction varies only very slowly in the outskirts of halos. This can be seen in Figure 3, where we show the radial profile of the baryon fraction for halos of different mass. While the sizes of halos can be systematically affected by different definitions of the virial radius (one may for example choose to use only the dark matter for the definition and not the total mass), the measured baryonic fractions are robust.

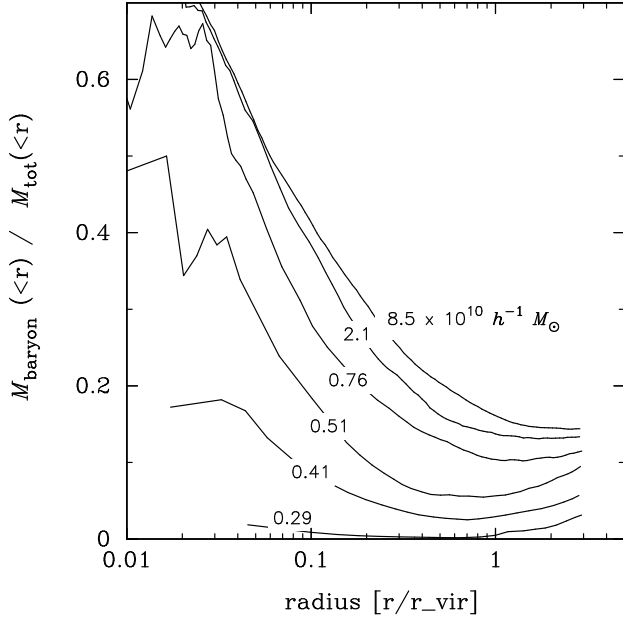


**Figure 3.** The baryon fraction as a function of radius for halos with different mass. All halos are chosen at  $z = 0$  from the basic simulation. Radii are normalised to the BDM virial radius. Labels along the lines indicate the mass of the halos.

The importance of the UV background for the baryon fraction is demonstrated in the right panels of Fig. 2, where we compare results of the ‘highUV’ and ‘lowUV’ simulations. Along with results from the ‘basic’ and ‘high-res’ runs (solid line) it can be seen that an increased UV-flux is able to evaporate the baryons in more massive halos. However, the dependence of this effect on the level of the UV is weak: two orders of magnitude difference in the UV-flux shifts the transition between ‘baryon-rich’ and ‘baryon-poor’ halos only by a factor of about two in mass.

Efficient stellar feedback can in principle also remove gas from small halos. However, for the thermal feedback considered in the multiphase feedback model used in our simulations, such a gas removal does not occur. While the feedback regulates the consumption of cold gas by star formation, it does not cause gaseous outflows. The latter only occur in our simulations if explicitly modeled with a kinetic feedback component (Springel & Hernquist 2003). However, we deliberately avoided the inclusion of such feedback models in this study, allowing us to focus on the impact of UV-heating in a clean fashion. Figure 2 (right panels) shows that in simulations without feedback the transition between ‘baryon-poor’ and ‘baryon-rich’ halos happens indeed virtually at the same place as in the ‘basic’ and ‘high-res’ runs.

We quantify the transition between the two extremes, ‘baryon-rich’ and ‘baryon-poor’, using a fitting function proposed by Gnedin (2000),

$$f_b = f_{b0} \left\{ 1 + (2^{\alpha/3} - 1) \left( \frac{M_c}{M_{\text{tot}}} \right)^{\alpha} \right\}^{-3/\alpha}, \quad (5)$$

where  $f_{b0}$  is the asymptotic baryon fraction in massive halos. Figure 4 indicates that a baryon fraction decreasing with mass can be reasonably well approximated assuming  $\alpha = 2$  in Eqn. (5). If one uses  $\alpha = 1$ , as advocated by Gnedin (2000), the transition to baryon poor halos is too shallow.

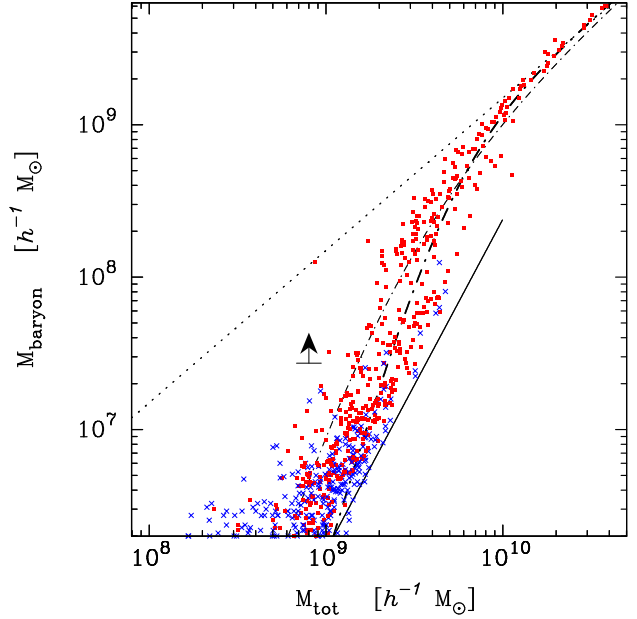


**Figure 4.** The baryon mass as a function of the total mass enclosed in the virial radius from the high-res run. Solid squares indicate halos with stars, and crosses those without. The dotted line shows the dependence if each halo would contain the mean cosmic baryon fraction. The solid line is derived based on the assumption that in low-mass halos the gas density follows the average distribution in the  $\rho$ - $T$  diagram (see Sec. 3.4 for more details). The arrow indicates a baryon mass consisting of 150 SPH particles. Thin and thick dash-dotted lines show the approximation of Eq. (5), with exponents  $\alpha = 1$  and  $2$ , respectively.

However, we note that for very small halos the approximation seems to fail in any case.

In the very massive halos of our samples we found a roughly constant baryon fraction  $f_{b0}$ , independent of redshift and numerical resolution. The value of  $f_{b0} \sim 0.16$  we measured lies slightly above the cosmic mean. At the characteristic mass,  $M_c$ , the baryon fraction is  $f_b = f_{b0}/2$  by definition. For  $z = 0$ , we derive a characteristic mass of  $M_c = 6.5 \times 10^9 h^{-1} M_{\odot}$  from the ‘high-res’ run. The lower panels of Fig. 2 show that this transition scale shifts to smaller masses at higher redshift.

In order to determine the evolution of  $M_c$  with redshift, we use a least-square fit of Eq. (5) to our measurements of the baryon mass fraction at a number of different simulation output times. We can infer the transition mass scale reasonably well from our simulations up to  $z \sim 5$ . In Figure 5, we show the resulting evolution of  $M_c(z)$ . Interestingly, as structure grows towards lower redshifts, progressively more massive halos become baryon-poor.

We note however that the characteristic masses inferred from our ‘basic’ simulation lie systematically above the values for the better resolved ‘high-res’ simulation. This difference can be due to several effects. First of all, lack of resolution can directly influence the results: at high redshifts ( $z \gtrsim 1.5$ ),  $M_c$  is below our assumed mass limit of well resolved halos (150 particles) for the ‘basic’ run, i.e.  $M_c$  has to be estimated from halos with  $M \geq M_c$  only. At  $z = 0$ , the difference in  $M_c$  from the two runs is still present. As can be seen in Figure 2, there are slightly more halos with inter-

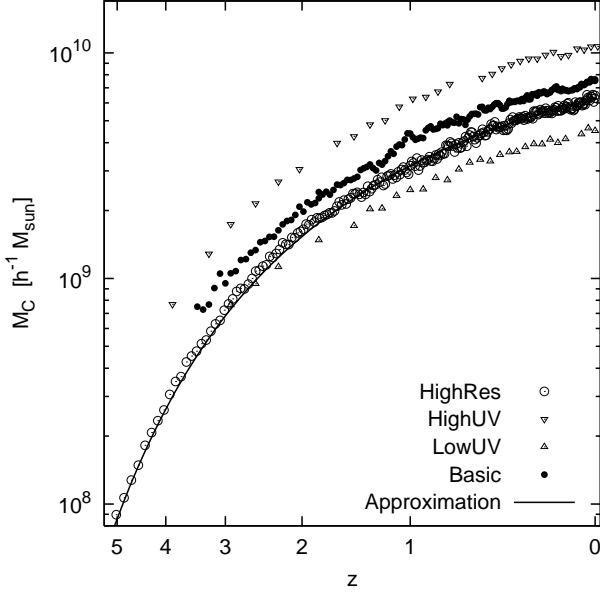


**Figure 5.** Evolution of the characteristic mass scale  $M_c$  for several simulations. We approximate the halo baryon fractions for each simulation by Eq. (5). We determine  $M_c$  using a least-squares method.  $f_{b0}$  is a free parameter, but it is almost constant for all simulations,  $f_{b0} \sim 0.16$ . Open circles and filled circles indicate the results for the basic and high-res simulations, respectively. Triangles indicate the results for a simulation with modified UV-flux. The solid line shows the approximation for  $M_c(z)$  from the high-res run using Eq. (6) and (7).

mediate baryon fractions when the resolution is improved. Again, lack of resolution has a strong impact on these halos around the transition region since they were significantly underresolved already at  $z \gtrsim 1.5$  in the ‘basic’ run. In contrast, in the ‘high-res’ run, these halos have been well resolved for a large redshift interval.

The evolution of the characteristic mass  $M_c(z)$  can be expressed as

$$\frac{M_c(z)}{10^{10} h^{-1} M_\odot} = \left\{ \tau(z) \frac{1}{1+z} \right\}^{3/2} \left\{ \frac{\Delta_c(0)}{\Delta_c(z)} \right\}^{1/2}, \quad (6)$$

where  $\tau(z)$  encodes the evolution of the minimum virial temperature required for halos to still allow further cooling in the presence of the UV background. We will discuss this criterion and its derivation in more detail below. Treating  $\tau(z)$  as a simple analytic fitting function for the moment, we find that our numerical results can be well described by

$$\tau(z) = 0.73 \times (z+1)^{0.18} \exp\{-(0.25z)^{2.1}\} \quad (7)$$

for the ‘high-res’ run over the entire redshift range, see Fig. 5.

### 3.3 How to suppress gas condensation

A quantitative understanding of the characteristic mass can be obtained by considering the equilibrium line between photo-heating rate and cooling rate in the density-temperature phase-space plane. In Figure 6, we show the gas particles at three different times, and include this equilibrium line for high-density gas, computed self-consistently

from the cooling and heating routines in GADGET. Much of the gas in the density range  $\delta \sim 10^3 - 10^6$  is indeed distributed along this line.

We define the equilibrium temperature at a fiducial overdensity of 1000 as ‘entry temperature’  $T_{\text{entry}}$  into the condensed phase. Gas that condenses in a halo will at least reach this temperature due to photo-heating before it can cool further to the  $\simeq 10^4$  K reached at very high overdensities. Note that this is independent of the potential difference between a ‘cold mode’ or a ‘hot mode’ of accretion (Keres et al. 2004). In the cold mode, gas creeps along the lowest possible temperature into the condensed phase, without being heated by an accretion shock to the virial temperature first, as it happens in the ‘hot mode’. However, even in the cold mode, the gas will at least be heated to the ‘entry temperature’  $T_{\text{entry}}$  by the UV background. After reaching this temperature, it can then evolve along the equilibrium line towards higher densities and eventually reach the onset of star formation. In a sense, for halos with  $T_{\text{vir}} = T_{\text{entry}}$ , the hot and cold mode should therefore become largely identical.

We argue that a comparison of  $T_{\text{vir}}$  with  $T_{\text{entry}}$  provides a simple criterion that tells us whether the gas in a halo can still cool. To demonstrate this, we show that this assumption provides a quantitative explanation for our measurements of  $M_c(z)$ . We define the virial temperature for our halos as

$$k_B T_{\text{vir}} = \frac{1}{2} \mu m_p \frac{G M_{\text{vir}}}{r_{\text{vir}}}, \quad (8)$$

where  $m_p$  is the proton mass and  $\mu$  is the mean weight of the fully ionised gas,  $\mu = 0.59$ . Virial mass and radius are related by the definitions of Eqs. (1) and (4). Hence the virial temperature depends on the mass as

$$T_{\text{vir}} = \frac{1}{2} \frac{\mu m_p}{k_B} \left\{ \frac{\Delta_c(z) \Omega_m}{2} \right\}^{1/3} (1+z) \{G M_{\text{vir}} H_0\}^{2/3}. \quad (9)$$

For the cosmological concordance model used here we insert  $\Omega_m = 0.3$  and cast Eq. (9) into

$$T_{\text{vir}} = 3.5 \times 10^4 \text{ K} (1+z) \left\{ \frac{\Delta_c(z)}{\Delta_c(0)} \right\}^{1/3} \left\{ \frac{M_{\text{vir}}}{10^{10} h^{-1} M_\odot} \right\}^{2/3}. \quad (10)$$

Now we apply our criterion introduced above: If the virial temperature of a halo is below the entry temperature into the condensed phase, its potential well is not deep enough to compress the gas sufficiently and to overcome the pressure barrier generated by the photo-heating. Thus, we expect that the characteristic halo mass necessary to increase the condensed baryonic mass can be estimated by rewriting Eq. (10) into

$$\frac{M_c(z)}{10^{10} h^{-1} M_\odot} \simeq \left\{ \frac{T_{\text{entry}}(z)}{3.5 \times 10^4 \text{ K}} \frac{1}{1+z} \right\}^{3/2} \left\{ \frac{\Delta_c(0)}{\Delta_c(z)} \right\}^{1/2}. \quad (11)$$

This result is the theoretical counterpart to the empirical fitting function introduced as Eq. (7).

In the following, we use the abbreviation  $\tilde{T}_{\text{entry}} = T_{\text{entry}}(z)/3.5 \times 10^4 \text{ K}$ . In Figure 7, we show the evolution of  $\tilde{T}_{\text{entry}}(z)$  for the high-res run and compare it with the expression for  $\tau(z)$  derived from fitting the measured redshift evolution of the characteristic mass in the same simulation. First of all, we note that the redshift variation of both is small compared with the evolution of the characteristic mass. This indicates that the large variation of the



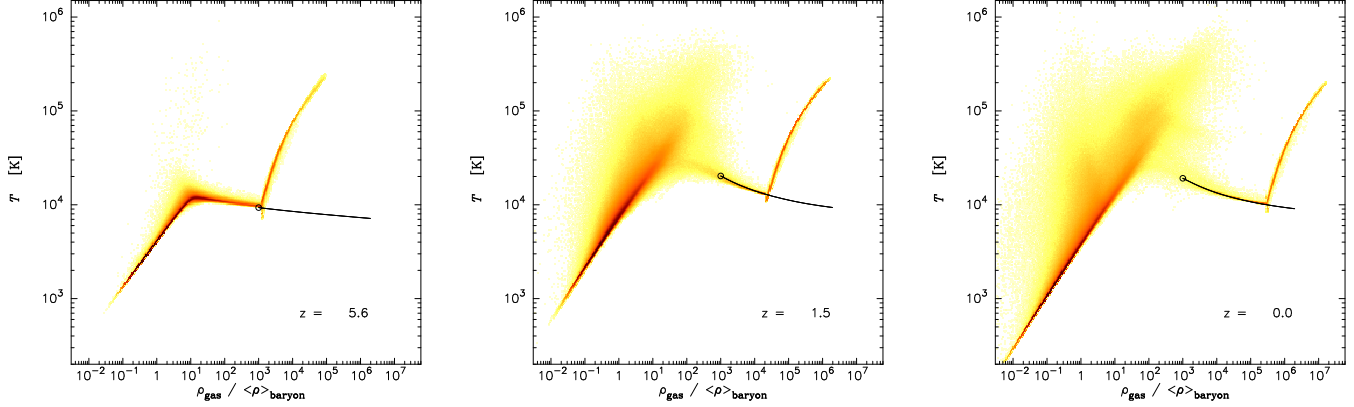


**Figure 6.** The distribution of particles in the density - temperature phase diagram for different redshifts for the high-res run. The solid curves give equilibrium line. It is derived from the heating-cooling module in the code by computing the temperature at which the heating rate equals the net cooling rate. We assume that the ‘entry’ into the condensed branch occurs at  $10^3 \langle \rho_{\text{baryon}} \rangle$ . The circles indicate the derived entry temperatures for the individual redshifts.

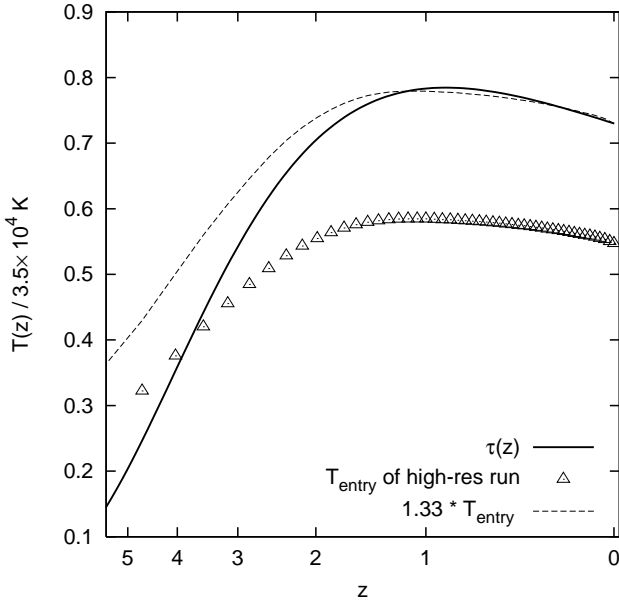


**Figure 7.** Evolution of the entry temperature. We derive from the high-res run the entry temperature,  $T_{\text{entry}}$ , for several redshifts (open triangles).  $T_{\text{entry}}$  is determined according to the description in the caption of Fig. 6. For comparison we plot the expression  $\tau(z)$  given in Eq. (7) (solid line). The scaled entry temperature (“refined model”) is also shown (dashed line).

latter is mainly governed by the  $1/(z+1)$  term in Eq. (6). Furthermore, from Fig. 7 we can conclude that the simple criterion invoked above reproduces the evolution of  $M_c(z)$  up to  $z \sim 5$  astonishingly well, with a deviation of a few 10 %.

However, the condition  $T_{\text{vir}} = T_{\text{entry}}$  appears to underestimate the characteristic mass for small redshift to some extent. This is not surprising for a number of reasons. For example, we compute the virial radius from the dark matter distribution only, hence the total masses used here are slightly above the virial masses. Furthermore,  $T_{\text{entry}}(z)$  de-

termined at a fixed overdensity 1000 may underestimate the true entry temperature. We can account for this and improve our match of the numerical results by refining our criterion in the following way: The virial temperature of a halo has to be  $\gtrsim 1.3 \times T_{\text{entry}}$  to permit further condensation.

To explain the deviation at high redshifts we have to acknowledge the fact that  $\tau(z)$  and  $\tilde{T}_{\text{entry}}$  are completely different in the sense that the latter denotes which halos are able to add more gas to the condensed phase at a given time, while the former reflects the entire evolution history of dwarf halos. Before reionisation, no halo is photo-evaporated, i.e.  $M_c = \tau = 0$ . It takes some time after reionisation to produce baryon-poor halos. Hence,  $\tau(z)$  should be below  $T_{\text{entry}}$  for some time after reionisation.

In any case, the agreement demonstrated in Figure 7 shows that the argument that the virial temperature should at least equal the entry temperature provides a good quantitative description for the transition scale between baryon-poor and baryon-rich halos. Interestingly, this explanation can account for the effect simply by alluding to the ongoing photo-heating of the gas by the UV-background radiation, and the accompanying increase of the gas pressure in low mass halos. At least at low redshift, the effects of the impulsive heating during the epoch of reionisation appear to play only a subdominant role.

### 3.4 Empty halos?

We argued above that photo-heating may prevent further gas condensation in dwarf halos. If it never takes place in a given halo, or an existing condensed phase has been evaporated at some time by the UV-background, the halo will only contain diffuse gas, where “diffuse” for our purposes denotes gas of too low density to support star formation. It is therefore also interesting to distinguish between halos with and without stars, as we have done in Fig. 4. This allows us to demonstrate again how closely the equilibrium line in the  $\rho$ - $T$  diagram, the virial temperature, and the baryon fraction are connected.

The expected baryonic mass in a halo is given by

$$M_b = \frac{4}{3} \pi r_{\text{vir}}^3 \bar{\rho}_b, \quad (12)$$



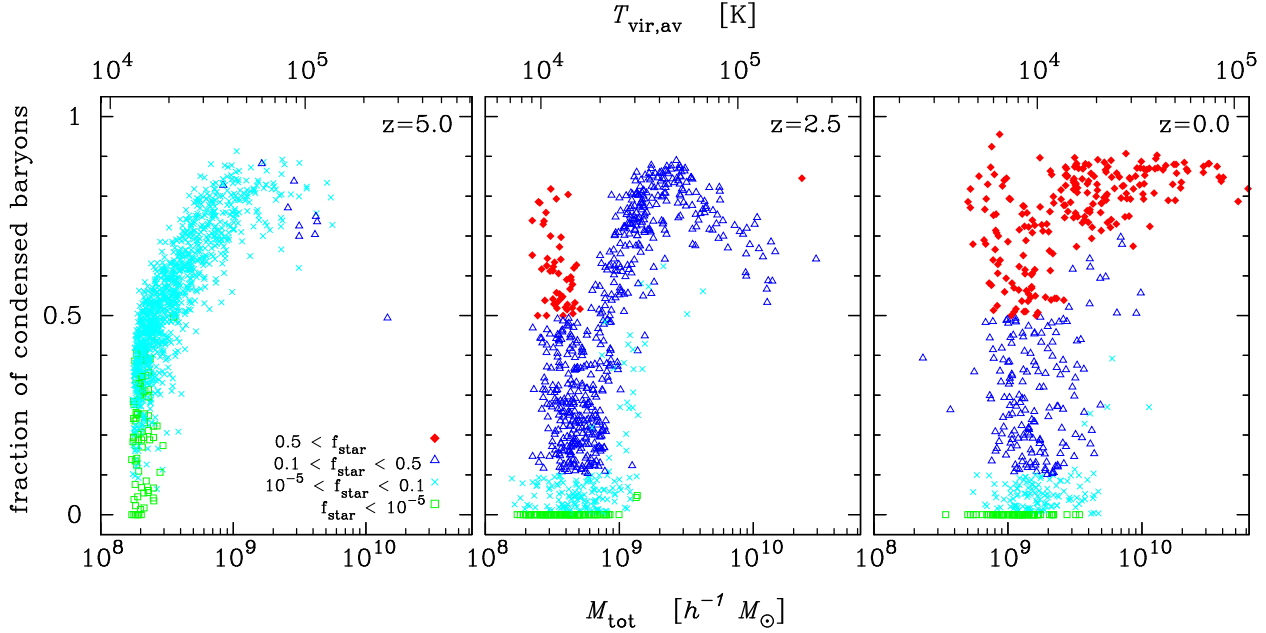


**Figure 8.** The baryon fraction in the condensed phase is shown for the halos of the high-res run. To the condensed phase belong the stellar mass and gas mass with  $\delta > 1000$  and  $T < 10^5$  K. The stellar fraction  $M_*/(M_* + M_{\text{gas,cond}})$  is distinguished by different symbols. Halos which contain less than 20 baryonic particles in the simulation are excluded.

where  $\bar{\rho}_b$  denotes the average gas density in a halo. At redshift  $z = 0$ , the majority of the gas is distributed at low densities along the power-law relation

$$\left(\frac{\rho_{\text{eq}}}{\langle \rho \rangle_b}\right)^{0.57} = \frac{T_{\text{eq}}}{3.6 \times 10^3 \text{ K}} \quad (13)$$

in the  $\rho$ - $T$  phase diagram, where photo-heating balances adiabatic cooling due to the expansion of the universe. If we assume that the average temperature in halos is given by the virial temperature, then the average density (of the diffuse gas) in a halo cannot lie below the relation given by Eq. (13), i.e. this imposes a rough upper limit on the average gas density, and hence the diffuse baryonic content of the halo. With the help of Eq. (10), we can replace the virial temperature by the virial mass and cast this condition for the average gas density in a halo into

$$\left(\frac{\bar{\rho}_b}{\langle \rho \rangle_b}\right)^{0.57} = 9.7 \times (z+1) \left\{ \frac{\Delta_c(z)}{\Delta_c(0)} \right\}^{\frac{1}{3}} \left\{ \frac{M_{\text{vir}}}{10^{10} h^{-1} M_\odot} \right\}^{\frac{2}{3}}. \quad (14)$$

Plugging this result into Eq. (12) and using the definition of the virial radius, Eq. (1), we obtain

$$\frac{M_b}{10^{10} h^{-1} M_\odot} = \frac{84.7}{\Delta_c(0)} \frac{\Omega_b}{\Omega_m} \left\{ \frac{M_{\text{vir}}}{10^{10} h^{-1} M_\odot} \right\}^{2.17}. \quad (15)$$

for the baryon mass at  $z = 0$ . The resulting baryon mass is shown in Fig. 4. Halos without any stellar matter are primarily distributed just above this line. Hence Eq. (15) provides a rough upper limit for the diffuse baryonic mass in dwarf-sized halos. In summary, for halos which contain virtually no condensed baryons, the diffuse gas mass can be determined from the equilibrium line in the  $\rho$ - $T$  phase diagram. This can hence explain why halos significantly below  $M_c$  are seemingly almost empty of gas.

Here we have implicitly assumed that the condensed

phase is eventually always converted into stars. It is however conceivable that some halos have a condensed phase without any stars. Figure 8 shows the fraction of condensed baryons

$$f_{\text{cond}} = \frac{M_{\text{gas,cond}} + M_*}{M_b}, \quad (16)$$

and also the stellar mass fraction. First of all, we see that in all halos with condensed baryons there are also stars. At  $z = 5.0$  virtually all halos cool gas and form stars. Later on, at  $z = 2.5$ , there are halos without any condensed baryonic phase (square symbols). The distribution can be subdivided into two groups: Halo with mass below  $\sim 7 \times 10^9 h^{-1} M_\odot$  (which corresponds at this redshift on average to  $T_{\text{vir}} \sim 2 \times 10^4$  K) have lost all their gas. This can be seen by the fact that  $f_{\text{star}} = 0.5$  occurs at  $f_{\text{cond}} = 0.5$ . More massive halos still have condensed gas. At  $z = 0$  the two groups are still present but more mixed. Concerning those halos free of condensed gas, Fig. 4 shows that the SPH particle number for the halos in question is not more than a few hundred. This indicates that condensed gas may be evaporated due to insufficient numerical resolution, despite the fact that these halos are composed by several thousand dark matter particles.

### 3.5 Condensation history

The basic argument above is that photo-ionisation can stop at some time the condensation process of gas in dwarf galaxy halos. We can support this idea further by finding halos with a constant amount of mass in the condensed phase. Figure 9 shows the evolution of the different mass components for two example halos. A halo selected with mass significantly above  $M_c$  at  $z = 0$  has continuously increased the dark matter, stellar, and condensed masses, while the gas mass de-

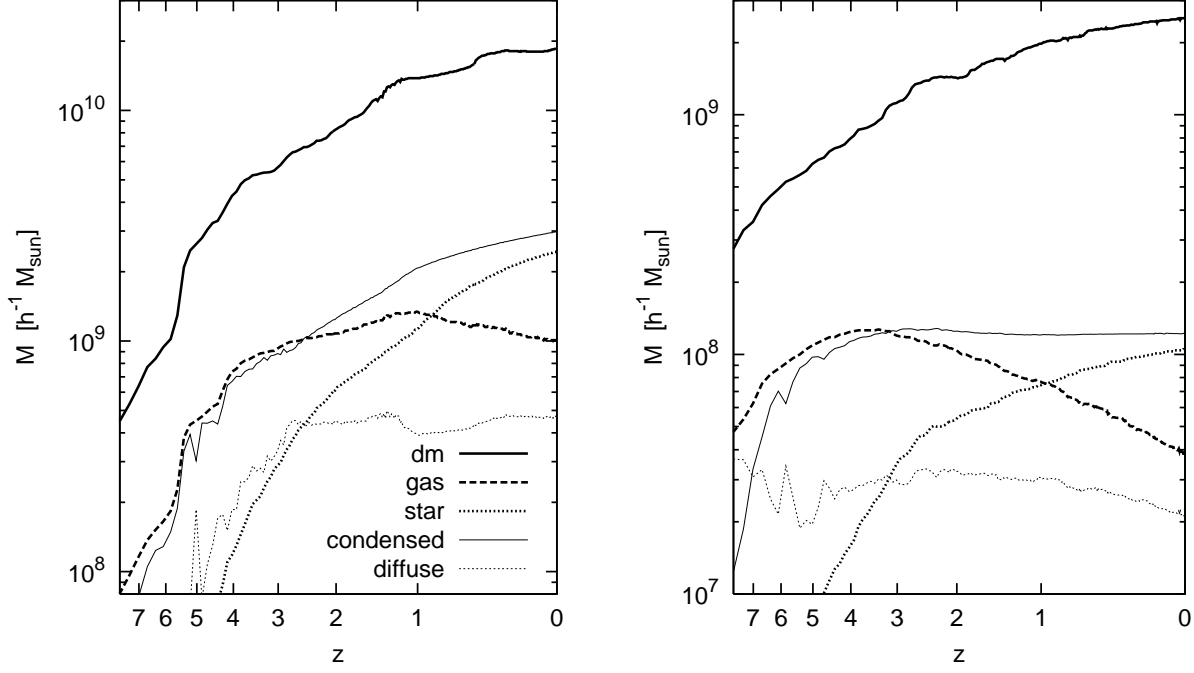


**Figure 9.** Evolution of the mass in different components for two high-resolution halos, one above  $M_c$  (left panel) and one below  $M_c$  (right panel). The evolution of the total mass (thick solid line), the condensed gas mass (thick dashed), the stellar mass (thick dotted) and diffuse gas mass (thin dotted) is shown. In addition the evolution of the condensed mass (gas+stars) is shown (thin solid line).

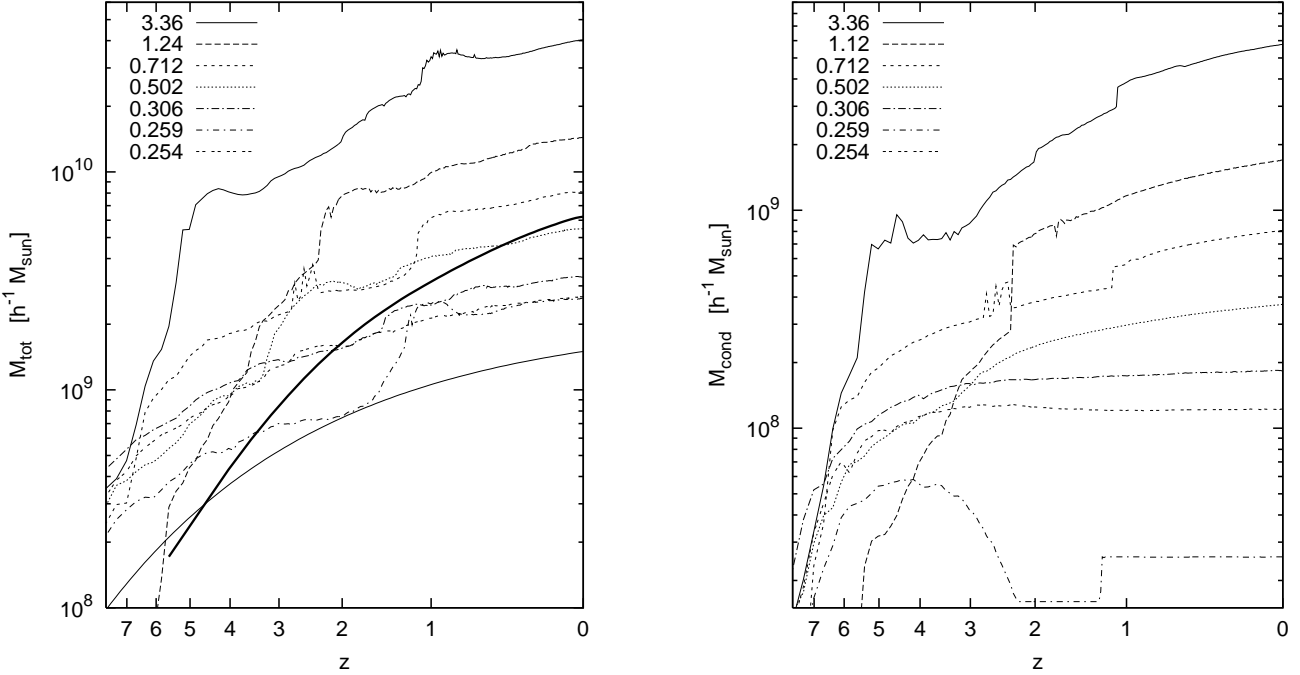


**Figure 10.** Mass accretion histories. We compute the mass accretion histories by choosing from the high-res run several halos at  $z = 0$  and searching repeatedly for the most massive progenitor. The left panel shows the evolution of the total mass, while the right panel shows the evolution of the condensed baryon mass of the same halos. Jumps in the condensed mass indicate merger events. The numbers indicate the dark matter mass at  $z = 0$  in  $10^{10} h^{-1} M_\odot$ . In the left panel, the evolution of the characteristic mass for the ‘high-res’ run is also shown (thick solid line). For comparison, we also plot the mean mass accretion history (thin solid line) for  $M_{\text{tot}} = 1.4 \times 10^9 h^{-1} M_\odot$  with  $\alpha = 0.35$ , as expected for a low density environment, see Eq. (17).

creased. In a halo with total mass significantly below  $M_c$ , the individual mass components change as well, but in contrast to the case of the more massive halo, the condensed mass is remarkably constant. This lends strong support to our basic argument. We see here that for the individual halo shown neither further gas condensates nor photo-heating evaporates all the gas. Thus even in the optically thin treatment of the galactic gas reservoir, photo-heating is not able to expel gas from the galaxy that has overdensities above  $\sim 1000$ . Instead, the condensed gas continues to be slowly converted into stars. It is thus not expected that photo-heating instantaneously switches off star formation.

We now analyse the mass accretion histories of several halos of different mass. In Fig. 10, we show that the evolution of the condensed phase changes systematically from halo masses below  $M_c$  to those above. For the latter, the total mass and the condensed mass grow almost in parallel. For halos with mass close to  $M_c$ , the condensed mass increases monotonically but slower than the total mass. Finally, for halos with mass significantly below  $M_c$ , the condensed mass remains constant. Thus the evolution of individual halos is perfectly consistent with the result that photo-heating primarily stops condensation in small halos. Moreover, we find that our ‘‘refined’’ criterion for condensation reproduces the time at which condensation stops quite well. To show this explicitly we have plotted in the left panel of Fig. 10  $M_c$  derived from  $T_{\text{vir}} = 1.3 \times T_{\text{entry}}$ . The times at which the low-mass halos fall below  $M_c$  correspond to the times at which the condensed masses begin to remain constant (right panel).

As already seen in Figure 8, the condensed phase is generally evaporated ‘in halos with  $M_{\text{tot}}(0) \lesssim 2 \times 10^9 h^{-1} M_\odot$ . Even if these halo appear to be sufficiently well resolved at  $z = 0$ , we caution that condensation can only take place at  $z \lesssim 4$ , and is at higher redshift since  $M(z) < M_c(z)$ . Hence we expect that in a simulation with higher resolution the condensed phase might stay and result in a noticeably larger amount of stars. However, we cannot really exclude that condensed gas in halos with  $M_{\text{tot}}(0) \lesssim 2 \times 10^9 h^{-1} M_\odot$  becomes generally unstable at some time and is therefore evaporated even for arbitrary good numerical resolution. Such an assumption is frequently invoked in simple analytic treatments. For instance, the analysis of Barkana & Loeb (1999) is based on the assumption that all gas with  $T > T_{\text{vir}}$  is evaporated. The fact that the significantly improved resolution of the ‘high-res’ run compared to the ‘basic’ run does not lead to a stable condensed gas phase in all halos with mass about  $M_{\text{tot}}(0) \sim 2 \times 10^9 h^{-1} M_\odot$  seems to point into this direction. However, more stringent test of this will require better resolution for the progenitor of these halos.

### 3.6 Stellar mass function

Using our estimates for the suppression of baryon condensation in halos with mass below  $M_c(z)$ , an approximation for the expected stellar content in small halos may be derived. To this end we assume a mean mass accretion history for the small halos in our sample. Wechsler et al. (2002) and van den Bosch (2002) showed that the average dark matter mass accretion histories can be approximated by

$$M_{\text{MAH}}(z) = M_{\text{tot}}(z=0) e^{-\alpha z}, \quad (17)$$

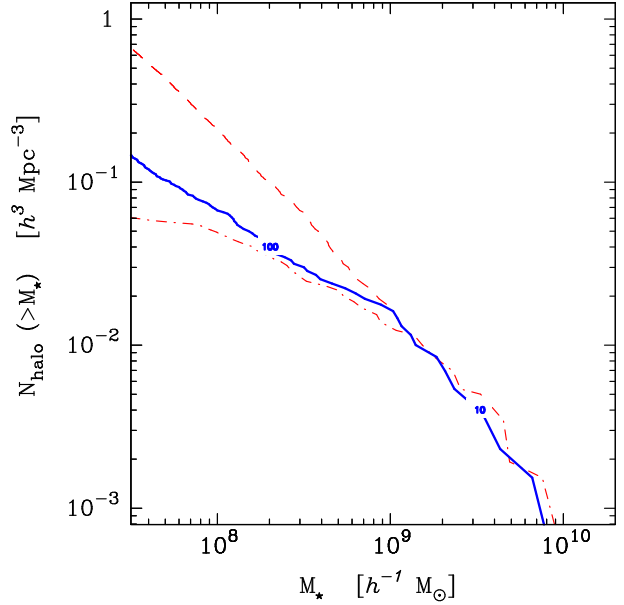


**Figure 11.** Stellar mass function at  $z = 0$ . We assign a stellar mass to each halo in the following manner: if  $M_{\text{tot}}(z=0) > M_c(0)$  the stellar mass is  $\langle f_* \rangle \Omega_b / \Omega_m M_{\text{tot}}$ . For smaller halos we compute the redshift  $z^*$  at which  $M_{\text{tot}} \exp(-\alpha z^*) = M_c(z^*)$ . We compute the stellar mass according to  $\langle f_* \rangle \Omega_b / \Omega_m M(z^*)$ . The solid line shows the results for the halo sample from the basic run and the parameters  $\langle f_* \rangle = 0.8$  and  $\alpha = 0.35$ . Numbers along the line indicate how many halos are actually in our void sample. For comparison the stellar mass function obtained from the simulation (dash-dotted) is shown. In addition, we show the result for the assumption that in each halo the stellar mass amounts to  $\langle f_* \rangle \Omega_b / \Omega_m M_{\text{tot}}$  (dashed line).

which works especially well for halos with an early formation time. In Fig. 10, we show an average accretion history (thin solid line) using  $\alpha = 0.35$ . Moreover, from the work of van den Bosch (2002) one can derive an appropriate value for  $\alpha$  for halos with  $\sim 5 \times 10^9 h^{-1} M_\odot$  in a low density universe.

All halos in our sample have rather flat accretion histories compared to the evolution of the characteristic mass  $M_c(z)$ , thus most of them have been able to condensate baryons and to form stars at high redshift. But at some time the halo mass fell below  $M_c(z)$ , and from this time onwards the mass in the condensed phase is expected to remain constant. To test this, we estimate the stellar mass in a halo by computing first the redshift  $z^{\text{eq}}$  at which the mass according to the accretion history equals the characteristic mass,  $M_{\text{MAH}}(z^{\text{eq}}) = M_c(z^{\text{eq}})$ . At this redshift, we determine the condensed mass, assuming here that at this time the baryon fraction in the halos has the cosmic mean value  $\Omega_b / \Omega_m$ . In addition, we assume that on average 80% of the baryons are in the condensed phase, see Fig. 8. Finally, as an upper limit for the amount of stars that may form, we assume that all of the condensed baryons are eventually converted into stars,  $\langle f_{\text{eq}} \rangle = 0.8$ . Hence we estimate the stellar mass in a given halo as  $M_{\text{eq}}(z=0) = \langle f_{\text{eq}} \rangle \Omega_b / \Omega_m M_{\text{MAH}}(z^{\text{eq}})$ . For halos more massive than  $M_c(z=0)$  the maximum stellar mass is given just by  $\langle f_{\text{eq}} \rangle \Omega_b / \Omega_m M_{\text{tot}}(0)$ .

We define the stellar mass function,  $N_{\text{halo}}(M_*)$ , as the number of halos with stellar mass larger than  $M_*$ , inde-

pendent of the dark matter masses of the halos that host the galaxies. Figure 11 shows the stellar mass function obtained by the procedure described above (solid line). For comparison, we also show the mass function for a fixed stellar mass fraction  $f_*$  for all halos (dashed line). The deviation of the two curves below  $M_* \sim 10^9 h^{-1} M_\odot$  indicates that in low-mass halos the stellar mass fraction falls below the fixed value  $f_*$ , hence those halos are shifted to smaller  $M_*$  and the mass function begins to flatten. For a stellar mass content of  $\sim 10^8 h^{-1} M_\odot$  the number of halos is reduced by a factor of three. The simulated halo sample (dash-dotted line) provides a lower limit for the stellar mass function because of the limited numerical resolution. Above  $\sim 10^8 h^{-1} M_\odot$ , the two curves agree very well. For smaller masses, the two curves deviate since some halos have formed too few stars due to insufficient resolution. In conclusion, the photo-evaporation reduces the number of halos with  $M_* \gtrsim 10^8 h^{-1} M_\odot$  by a factor of about four and, more importantly, the faint-end slope of the stellar mass function is much shallower than expected based on the dark halo mass function of  $N$ -body simulations alone.

#### 4 DISCUSSION

The main purpose of this work has been to investigate the effect of UV-heating on the baryon fraction and the stellar mass of dwarf-sized isolated halos in voids. This is motivated by the suggestion that photo-heating may provide a potential explanation for the observed low number density of galaxies in voids, and the apparent paucity of luminous galactic satellites in the Local Group, in contrast to the large abundance of dark matter halos and subhalos, respectively, predicted by CDM models.

In order to examine this question, we have carried out some of the presently best resolved hydrodynamical simulations of galaxy formation in large regions of space. Our simulations are unique in the sense that they specifically sample cosmological void regions at high resolution and evolve them to the present epoch.

We have identified a characteristic mass scale below which the baryon fraction in a halo is reduced by photo-heating. This happens for masses  $M_{\text{vir}}(z=0) \lesssim 6.5 \times 10^9 h^{-1} M_\odot$  (denoted here as dwarf galaxies), and this characteristic mass scale depends only weakly on the UV-flux. The suppression itself happens due to photo-evaporation of gas out of halos, thereby reducing the baryon fraction of dwarf galaxies, and also by offsetting cooling losses in halos such that further condensation of baryons is strongly reduced. We have derived a simple quantitative criterion that gives the characteristic mass  $M_c$  at which the baryon fraction is on average half that of the cosmic mean. This is phrased on a condition on the virial temperature which must at least reach an “entry temperature” in the unstable branch of the cooling/heating equilibrium line in the gas phase-space diagram. Our prediction for  $M_c(z)$  is strikingly well in accord with the evolution obtained from the simulations.

At redshift  $z=0$ , the characteristic mass scale of photo-evaporation corresponds to a circular velocity of  $\sim 27 \text{ km s}^{-1}$ , which is significantly less than we would obtain with the filtering mass formalism introduced by Gnedin

(2000) using an entirely different approach. We thus predict a considerably milder effect of photo-heating on the evolution of small halos. This has significant consequences for semi-analytic models of galaxy formation that relied on photo-heating as a feedback mechanism to suppress small galaxies. For instance, Somerville (2002) concluded that the substructure problem in the Local Group can be easily solved taking photo-evaporation into account, provided the effect is as strong as suggested by the analysis of Gnedin (2000). This conclusion is probably no longer valid when the effect is much weaker, as we find here.

It is clear however that the baryon fraction and hence the star fraction rate in void dwarf galaxies is significantly reduced by the UV-background. As a result, the halo mass function cannot be translated directly into a mass function of the luminous matter. In the framework of the physics included in our simulations, we argue that the baryonic mass belonging to a halo is essentially set at the time when  $M_{\text{vir}}(z) = M_c(z)$ . We compute the resulting mass function of the stellar content in halos under this assumption and obtain good agreement with our direct simulation measurements.

We caution however that it is numerically difficult to resolve all the star formation in small dwarf galaxies at high redshift. While we have found some dwarf halos in our simulation without any stars, it seems plausible that this is due to insufficient resolution, because all halos with a progenitor with  $M(z) > M_c(z)$  at some  $z$  should have been able to create some stars. Only in those halos with a very steep mass accretion history, steep enough to be for all redshifts below  $M_c(z)$ , star formation should always be suppressed.

Our results are derived under the assumption of optically thin gas with a spatially uniform UV flux, neglecting any effects due to self-shielding in the inner parts of halos. Recently, Susa & Umemura (2004b) analysed photo-evaporation with 3D radiation transfer simulations for individual halos. They found that for both a full radiation transfer treatment and a optical thin approximation the fast rising UV-background at high redshift efficiently suppresses star formation. However, a full radiation transfer treatment with self-shielding can only increase the amount of stars because it makes the UV heating less efficient. Neglecting self-shielding in our analysis may thus lead to an *overestimate* of the effects of the UV-background.

Our result do depend strongly on the UV-flux history. We have here used the Haardt & Madau (1996) model, where reionisation takes place at redshift  $z=6$ . The recent WMAP (Spergel et al. 2003) results point to a much earlier beginning of the epoch of reionisation. If true, the evolution of  $M_c$  could be much more shallow at high redshift. Consequently more halos would have an accretion history steeper than  $M_c(z)$ , and hence more halos should remain virtually free of condensed baryons.

However, it appears unlikely that these adjustments in the reionisation history can alter our basic finding that UV-heating is not particularly efficient in evaporating all baryons out of dwarf-sized halos. This makes it questionable whether feedback by photo-heating is really sufficient to suppress dwarf galaxies in voids, luminous satellites in galaxies, and to flatten the faint end of the galaxy luminosity function as much as observationally indicated. Other proposed solutions like kinetic supernova feedback and as-

sociated galactic winds may therefore be needed to resolve these problems completely.

## ACKNOWLEDGEMENTS

This work has been partially supported by the Acciones Integradas Hispano-Alemanas. MH and GY thanks financial support from the Spanish *Plan Nacional de Astronomia y Astrofisica* under project number AYA2003-07468. This research was supported in part by the National Science Foundation under Grant No. PHY99-0794. GY and SG thanks the Kavli Institut for Theoretical Physics for hospitality. We thank the John von Neumann Institute for Computing (Germany), the CIEMAT at Madrid (Spain), and the CLAMV at IU Bremen for kindly allowing us to use their computational facilities.

## REFERENCES

- Abel T., Bryan G. L., Norman M. L., 2000, *ApJ*, 540, 39
- Babul A., Rees M. J., 1992, *MNRAS*, 255, 346
- Barkana R., Loeb A., 1999, *ApJ*, 523, 54
- Bryan G. L., Norman M. L., 1998, *ApJ*, 495, 80
- Couchman H. M. P., Rees M. J., 1986, *MNRAS*, 221, 53
- Dekel A., Rees M. J., 1987, *Nature*, 326, 455
- Dekel A., Silk J., 1986, *ApJ*, 303, 39
- Efstathiou G., 1992, *MNRAS*, 256, 43
- Gnedin N. Y., 2000, *ApJ*, 542, 535
- Goldberg D., Jones T., Hoyle F., Rojas R., Vogeley M., Blanton M., 2004, Accepted to *Astrophysical Journal*
- Gottlöber S., Klypin A. A., Kravtsov A. V., Turchaninov V., 1999, in Banday A., Sheth R. K., Dalosta L. N., eds, *Evolution of Large Scale Structure : From Recombination to Garching Evolution of isolated halos and halos inside of groups and clusters in a LambdaCDM model*. pp 358–
- Gottlöber S., Lokas E. L., Klypin A., Hoffman Y., 2003, *MNRAS*, 344, 715
- Grebel E. K., Gallagher J. S., 2004, *ApJL*, 610, L89
- Gregory S. A., Thompson L. A., 1978, *ApJ*, 222, 784
- Grogin N. A., Geller M. J., 1999, *AJ*, 118, 2561
- Haardt F., Madau P., 1996, *ApJ*, 461, 20
- Hoffman Y., Shaham J., 1982, *ApJL*, 262, L23
- Joeveer M., Einasto J., Tago E., 1978, *MNRAS*, 185, 357
- Keres D., Katz N., Weinberg D. H., Dave R., 2004, *ArXiv Astrophysics e-prints* 0407095
- Kirshner R. P., Oemler A., Schechter P. L., Shectman S. A., 1981, *ApJL*, 248, L57
- Klypin A., Gottlöber S., Kravtsov A. V., Khokhlov A. M., 1999, *ApJ*, 516, 530
- Klypin A., Kravtsov A. V., Bullock J. S., Primack J. R., 2001, *ApJ*, 554, 903
- Kravtsov A. V., Gnedin O. Y., Klypin A. A., 2004, *ApJ*, 609, 482
- Kuhn B., Hopp U., Elsaesser H., 1997, *A&A*, 318, 405
- Lindner U., Einasto M., Einasto J., Freudling W., Fricke K., Lipovetsky V., Pustilnik S., Izotov Y., Richter G., 1996, *A&A*, 314, 1
- Mac Low M., Ferrara A., 1999, *ApJ*, 513, 142
- Machacek M. E., Bryan G. L., Abel T., 2001, *ApJ*, 548, 509
- Mateo M. L., 1998, *ARA&A*, 36, 435
- Mathis H., White S. D. M., 2002, *MNRAS*, 337, 1193
- Moore B., Ghigna S., Governato F., Lake G., Quinn T., Stadel J., Tozzi P., 1999, *ApJL*, 524, L19
- Navarro J. F., Steinmetz M., 1997, *ApJ*, 478, 13
- Navarro J. F., Steinmetz M., 2000, *ApJ*, 538, 477
- Peebles P. J. E., 1982, *ApJL*, 263, L1
- Peebles P. J. E., 2001, *ApJ*, 557, 495
- Popescu C. C., Hopp U., Elsaesser H., 1997, *A&A*, 325, 881
- Power C., Navarro J. F., Jenkins A., Frenk C. S., White S. D. M., Springel V., Stadel J., Quinn T., 2003, *MNRAS*, 338, 14
- Rees M. J., 1986, *MNRAS*, 218, 25P
- Somerville R. S., 2002, *ApJ*, 572, L23
- Spergel D. N., Verde L., Peiris H. V., Komatsu E., Nolte M. R., Bennett C. L., Halpern M., Hinshaw G., Jarosik N., Kogut A., Limon M., Meyer S. S., Page L., Tucker G. S., Weiland J. L., Wollack E., Wright E. L., 2003, *ApJS*, 148, 175
- Springel V., Hernquist L., 2002, *MNRAS*, 333, 649
- Springel V., Hernquist L., 2003, *MNRAS*, 339, 289
- Springel V., Yoshida N., White S. D. M., 2001, *New Astronomy*, 6, 79
- Susa H., Umemura M., 2004a, *ArXiv Astrophysics e-prints* 0406305
- Susa H., Umemura M., 2004b, *ApJ*, 600, 1
- Tassis K., Abel T., Bryan G. L., Norman M. L., 2003, *ApJ*, 587, 13
- Thoul A. A., Weinberg D. H., 1996, *ApJ*, 465, 608
- Umemura M., Ikeuchi S., 1984, *Prog. Theor. Phys.*, 72, 47
- van de Weygaert R., van Kampen E., 1993, *MNRAS*, 263, 481
- van den Bosch F. C., 2002, *MNRAS*, 331, 98
- Wechsler R. H., Bullock J. S., Primack J. R., Kravtsov A. V., Dekel A., 2002, *ApJ*, 568, 52
- Yepes G., Kates R., Khokhlov A., Klypin A., 1997, *MNRAS*, 284, 235